



# Structural Analysis of a Wind Turbine Blade Repurposed as an Electrical Transmission Pole

Ammar A. Alshannaq, S.M.ASCE<sup>1</sup>; Lawrence C. Bank, Dist.M.ASCE<sup>2</sup>; David W. Scott, M.ASCE<sup>3</sup>; and T. Russell Gentry<sup>4</sup>

**Abstract:** This paper focuses on the conceptual use of a fiber-reinforced polymer (FRP) wind turbine blade that is repurposed for a second life as an electrical transmission pole. Thousands of tons of fiber-reinforced polymer composite wind turbine blades are currently coming out of service globally and are being landfilled or incinerated. These are not environmentally preferable disposal methods. This paper presents a detailed structural analysis of a Clipper C96, 46.7-m-long turbine blade used as an electrical pole. The analytical procedure needed to characterize the wind turbine blade for repurposing includes determining the external and internal geometry of the blade, identifying the types of materials and laminates used throughout the blade, and calculating effective moduli and section properties for structural analysis. Code-specified load combinations are then used to analyze the transmission line *BladePole* to determine internal forces and deformations and stresses. Maximum stresses were compared to those obtained from theoretical models. The results indicate that wind turbine blades can safely be used as electrical transmission poles. **DOI:** 10.1061/(ASCE)CC.1943-5614.0001136. © 2021 American Society of Civil Engineers.

**Author keywords:** Repurpose; Fiber-reinforced polymer (FRP); Electrical power transmission structures; Structural analysis; Wind turbine blade.

#### Introduction

Wind turbine blades are structures made primarily from glass fiberreinforced polymer (GFRP). Typically, three of these blades are connected to a central hub that rotates with the wind to power a turbine that generates electricity. The manufacturing techniques involved in the process of wind blade production have been improved over the years, starting with wet hand layup techniques and progressing through filament winding, prepreg technology, and vacuum-assisted resin transfer molding (VARTM), which has improved the production quality extensively (Brøndsted et al. 2005). The main problem with these structures is their service life (approximately 20 years) limited primarily by fatigue damage from transient wind loading (Hayman et al. 2008). In some cases, wind blades are retired before their 20-year design life due to the need to upgrade wind farms to increase electrical generation referred to as re-powering of wind farms. A blade's mass follows an approximately third-degree exponential increase as a function of blade length (Brøndsted et al. 2005). Given the number of

<sup>1</sup>Graduate Student, School of Civil and Environmental Engineering, Georgia Institute of Technology, 790 Atlantic Dr, Atlanta, GA 30332. ORCID: https://orcid.org/0000-0002-3455-3784. Email: aalshannaq3@gatech.edu

<sup>2</sup>Research Faculty, School of Architecture, Georgia Institute of Technology, 245 4th St NW, Atlanta, GA 30332 (corresponding author). Email: larry.bank@design.gatech.edu

<sup>3</sup>Professor and Chair, Dept. of Civil Engineering and Construction, Georgia Southern Univ., P.O. Box 8077, Statesboro, GA 30460. Email: dscott@georgiasouthern.edu

<sup>4</sup>Associate Professor, School of Architecture, Georgia Institute of Technology, 245 4th St NW, Atlanta, GA 30332. Email: russell.gentry@design.gatech.edu

Note. This manuscript was submitted on September 22, 2020; approved on March 13, 2021; published online on April 28, 2021. Discussion period open until September 28, 2021; separate discussions must be submitted for individual papers. This paper is part of the *Journal of Composites for Construction*, © ASCE, ISSN 1090-0268.

wind turbines in operation and nearing their end-of-service life, it is anticipated that millions of tons of blade waste will need to be disposed of in the next 20 years (Liu and Barlow 2017).

In addition to their use in wind blades over the past 30 years, pultruded and molded GFRP materials are also routinely used in load-bearing civil and infrastructure engineering applications due to their beneficial properties, including high strength-to-weight ratios, high stiffness-to-weight ratios, durability, and corrosion resistance (Bank 2006). The use of FRP materials to retrofit and reinforce concrete structures has been widespread over the last few decades (Bank 2006). These materials have proven their performance in civil engineering infrastructure, which suggests that wind blades may be attractive as construction materials in less demanding second-lives after their limited first-life uses as aerodynamic structures.

The current research program, entitled Re-Wind (Re-Wind Network 2021), is investigating adaptive repurposing options of these structures and materials in second-life applications. Numerous alternatives for repurposing have been proposed (Bank et al. 2018a). One proposes the use of cut parts from wind blades as affordable housing solutions (e.g., rooftops, window shutters and doors, and elevated platforms in flood regions), (Bank et al. 2018b; Gentry et al. 2018, 2020). Another proposes the use of two full-scale V-29 wind blades as girders for a pedestrian bridge, where structural detailing was completed and strength utilization ratios showed reasonable safety margins (Suhail et al. 2019). The feasibility of wind blades as electrical transmission structures was first proposed by Alshannaq et al. (2019), who presented preliminary results that indicate that working stresses will be below design allowables in the wind blade composites. The electrical transmission application is considered promising for wind blade repurposing for three main reasons: (1) the cantilever nature of the pole is similar to the blade's first-life use; (2) the load levels are much lower compared to the wind loads in their use in wind turbines; and (3) the poles will likely exhibit significant durability against environmental attack (Katnam et al. 2015). Moreover, there are currently a number of FRP transmission poles in the market [e.g.,

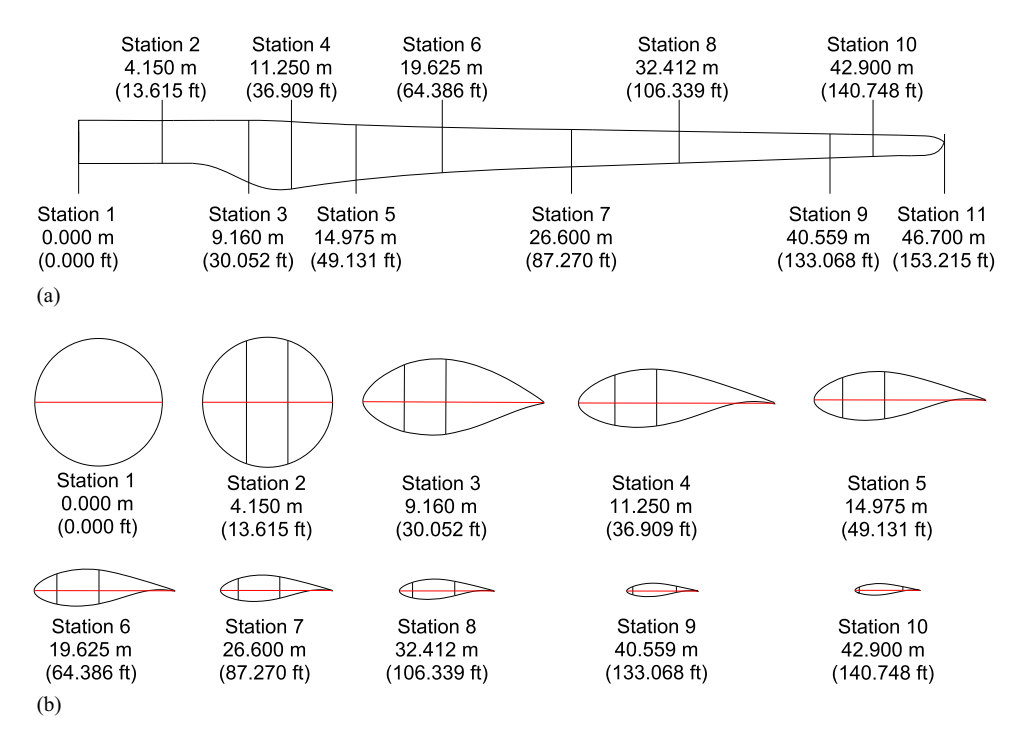


Fig. 1. Clipper C96 blade details: (a) stations along the blade; and (b) airfoil shapes at the stations along the length.

RS Poles—(RS 2021)] and there is an ASCE guide that addresses FRP transmission poles (Task Committee on Fiber-Reinforced Polymer Products for Overhead Utility Line Structures 2019). The rationale for using FRP poles (or FRP blades as poles) include lightweight (can be installed using helicopters, for example), corrosion resistance, electromagnetic transparency (leading to shorter crossarm lengths), and ease of installation.

This paper aims to lay the groundwork for a future reliability-based design methodology for a wind blade as a repurposed civil structure using the electrical transmission pole as an example. There are transmission poles, frames, and towers made of latticed steel members, hollow steel sections, prestressed concrete, timber, and FRP, and hundreds of different configurations and designs available (Power Line Systems 2021). The most significant design consideration for the wind blade pole relative to the existing monopoles is that the blades are not axisymmetric as are most other monopoles. Thus, the analysis described in the paper is necessarily somewhat complex. However, nonsymmetric thin-walled structures are common in structural engineering practice and present no inherent analytical difficulty.

### **Cross Section of a Clipper C96 Wind Turbine Blade**

The wind turbine blade considered for this study was a 46.7-m-long Clipper C96 blade. The Clipper Windpower Company that produced the Clipper blades is no longer in business as a blade manufacturer; however, their blades are representative of many blades manufactured in the 2001–2010 decade. Many of the Clipper blades are or will be coming out of service. The blade geometry and internal structure are shown schematically at 10 stations along the length in Figs. 1(a and b). As can be seen, the hollow, multicellular cross-sectional shapes start with a circular cross section at the left end (which is called the root in the wind blade industry) and then transition into an airfoil shape that culminates at the right end (which is called the tip). The purpose of the root region is to connect the blade to a rotating hub connected to the turbine

and gearbox. The root is primarily *structural* and resists the large bending forces that are generated from the wind pressure on the cantilevering blade. The primary purpose of the airfoil region (from Station 5 to the tip) is *aerodynamic* and this section captures the wind to generate lift and spin the three-bladed rotor. The total distance from the leading edge to the trailing edge is called the *chord length* and is shown in Fig. 1(b) by the horizontal lines (the lines connecting the right side to the left side of the cross section). The internal shear webs that run down the length of the blade are shown by the two vertical lines in Fig. 1(b). As it can be seen, the chord length reaches a maximum value of 3.71 m in the region between Stations 3 and 4 for the Clipper C96 blade.

A typical cross section of the wind blade is shown in Fig. 2. Three distinct parts can be seen: the shell, the spar caps, and the webs. The shell, which is a sandwich layup of thin triaxial GFRP skins and a balsa wood core, is manufactured in two halves joined at the leading and trailing edges. The webs (front and rear webs) are also sandwich layups of biaxial GFRP materials and a balsa core. The upper and lower spar caps are made primarily from uniaxial GFRP composites that provide the load-bearing capacity in bending.

#### Material Characterization of the Clipper C96 Blade

The Clipper C96 blade is made from different GFRP composite layups (i.e., uniaxial, biaxial, and triaxial). To characterize these composites, the stacking sequence needs to be determined. In general, due to the proprietary nature of these blade structures, the material types and stacking sequences are not known a priori. However, for the current project, the original OEM (original equipment manufacturer) fabrication plans and layup schedules were made available to the research team. In the general case, where OEM plans are not available, destructive test methods such as cutting sections and conducting burnout tests according to ASTM D2584 (ASTM 2018) need to be conducted at different locations to get the thicknesses, material types, and stacking sequences.

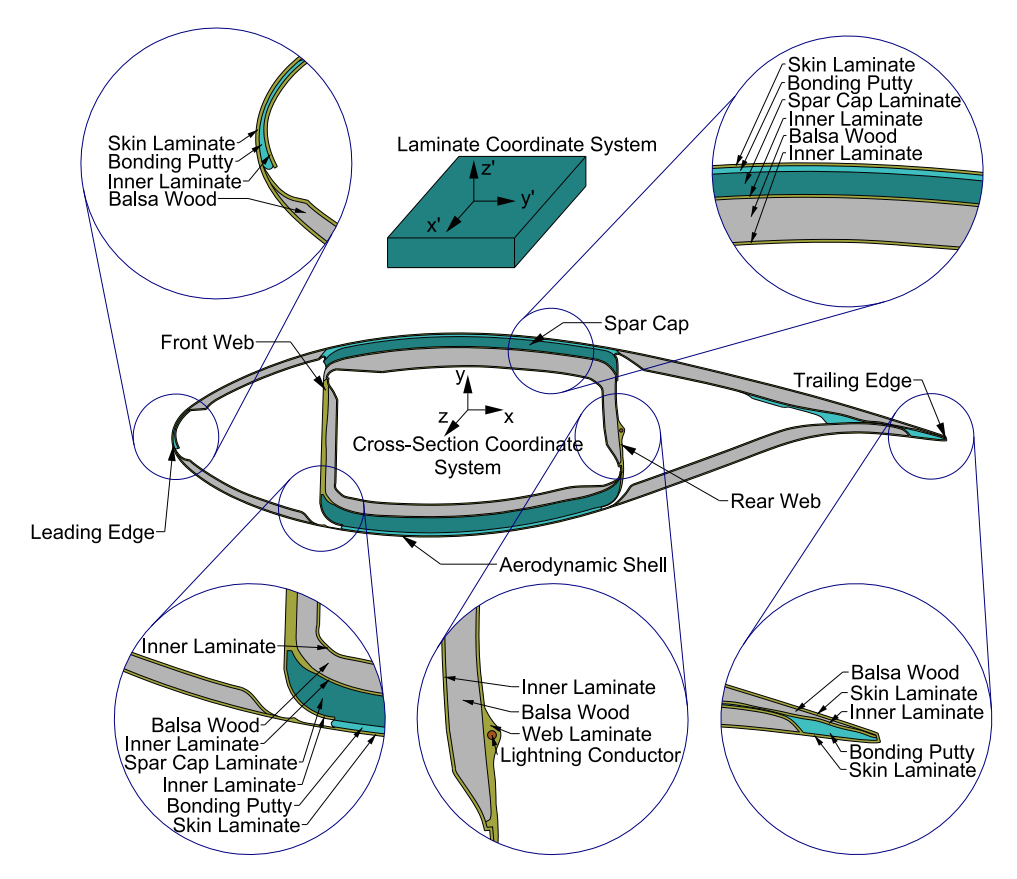


**Fig. 2.** Typical cross section of the Clipper C96 wind turbine blades taken from OEM (original equipment manufacturer) plans. The cross section at the root omits the webs and balsa cores. x' is in the laminate longitudinal direction (parallel to the blade section z-direction), y' is in the laminate transverse direction, and z' is in the laminate thickness direction.

For the current work, the OEM layup schedules and fiber volume fractions at specific locations were verified using the ASTM burnout tests. The fiber volume fraction of the spar cap laminate (primarily unidirectional) obtained from burnout tests was  $V_f = 50\%$ . The shell and web laminates had measured volume fractions of  $V_f = 28.6\%$  and  $V_f = 38.4\%$ , respectively.

## Effective Stiffnesses of the Clipper C96 Blade

In what follows, the BladePole is modeled using one-dimensional (1D) beam elements [with axial, bending, and torsional deformations—also called framework element by McGuire et al. (2000)] in a structural analysis frame program. Therefore, the effective cross-sectional properties at the different stations along the length need to be calculated first. Using the OEM provided stacking sequences and the fiber types, Helius Composite (Autodesk 2016) commercial FRP composites software was used to predict the mechanical properties of the laminate. Stiffnesses and strengths of different laminates forming the cross section (i.e., the shell, the spar caps, and the webs) were predicted at all stations shown in Fig. 1. The lamina used in Helius to model the individual lamina in the wind blade laminates (uniaxial, biaxial, and triaxial) with the stacking sequences taken from the OEM data was an E-glass/epoxy lamina with a volume fraction of  $V_f = 50\%$ , which was equal to the measured volume fraction in the spar cap. The properties of the epoxy matrix and the E-glass fiber used to model the lamina are

**Table 1.** Mechanical properties of epoxy matrix

Matrix commercial name	E (MPa)	G (MPa)	<i>v</i> (—)	ρ (g/ cm <sup>3</sup> )	$\sigma_t$ (MPa)	$\sigma_c$ (MPa)	τ (MPa)
EPIKOTE Resin MGS RIMR 135	2,950	1,160	0.27	1.19	67.5	85.0	37.5

Source: Adapted from Metyx Composites (2020).

Note: E = Young's modulus; G = shear modulus; v = Poisson's ratio;  $\rho = \text{density}$ ;  $\sigma_t = \text{tensile strength}$ ;  $\sigma_c = \text{compressive strength}$ ; and  $\tau = \text{shear strength}$ .

Table 2. Mechanical properties of E-glass fiber

E (MPa)	G (MPa)	v (—)	$\rho$ (g/cm <sup>3</sup> )	$\sigma_t$ (MPa)	$\sigma_c$ (MPa)
72,400	30,167	0.20	2.60	2,150	1,450

Source: Adapted from Matweb (2020).

Note: E = Young's modulus; G = shear modulus; v = Poisson's ratio;  $\rho = \text{density}$ ;  $\sigma_t = \text{tensile strength}$ ; and  $\sigma_c = \text{compressive strength}$ .

summarized in Tables 1 and 2, respectively. It is important to note that the web and the shell are composed of sandwich structures that were not modeled in this study and are the subject of ongoing work.

The areas, centroids, and moments of inertia of the different parts (i.e., the shell, the spar caps, and the webs) of the irregularly shaped cross sections were determined via built-in functions in AutoCAD (Autodesk 2019).

With the mechanical properties and the area properties, the effective stiffnesses of the cross sections can be determined as follows:

1. Determine the centroidal area properties (i.e., area and moment of inertia) using AutoCAD for each part then use Eqs. (1) and (2) to determine the centroid of the composite section:

$$E_{\text{Shell}} \int_{A_{\text{Shell}}} y dA + E_{\text{Web}} \int_{A_{\text{Web}}} y dA + E_{\text{Spar Cap}} \int_{A_{\text{Spar Cap}}} y dA = 0 \quad (1)$$

$$E_{\rm Shell} \int_{A_{\rm Shell}} x dA + E_{\rm Web} \int_{A_{\rm Web}} x dA + E_{\rm Spar\,Cap} \int_{A_{\rm Spar\,Cap}} x dA = 0 \quad (2)$$

where  $E_{\rm Shell}$ ,  $E_{\rm Spar\ Cap}$ , and  $E_{\rm Web} = E_{x'x'}$  for the laminate of the shell, the spar cap, and the web, respectively; and  $A_{\rm Shell}$ ,  $A_{\rm Spar\ Cap}$ , and  $A_{\rm Web} =$  areas of the shell, the spar cap, and the web, respectively.

2. Use the parallel-axis theorem to determine the moment of inertia about the composite centroid using Eqs. (3)–(5) in which *i* represents the specific part (i.e., the shell, the spar caps, and the webs):

$$I_{xx,i} = I_{xxc,i} + A_i d_{y,i}^2 \tag{3}$$

$$I_{yy,i} = I_{yyc,i} + A_i d_{x,i}^2 \tag{4}$$

$$I_{xv,i} = I_{xvc,i} + A_i d_{x,i} d_{v,i}$$

$$\tag{5}$$

where  $I_{xx,i}$  and  $I_{yy,i}$  = moments of inertia of the *i*th part about the composite centroidal x-axis and y-axis, respectively;  $I_{xxc,i}$  and  $I_{yyc,i}$  = moments of inertia of the *i*th part about the part's centroidal x-axis and y-axis, respectively;  $I_{xy,i}$  = product moment of inertia of the *i*th part about the composite centroidal x-axis and y-axis;  $I_{xyc,i}$  = product moment of inertia of the *i*th part about the part's centroidal x-axis and y-axis;  $A_i$  = area of the *i*th part;  $d_{x,i}$  = distance from the part's centroidal y-axis to the composite centroidal y-axis of the *i*th part; and  $d_{y,i}$  = distance from the part's centroidal x-axis of the *i*th part.

3. Determine the stiffnesses EA,  $(EI)_{xx}$ ,  $(EI)_{yy}$ , and  $(EI)_{xy}$  by multiplying each part's stiffness with its corresponding area or moment of inertia. Finally, summing the contribution of each part gives the effective cross-sectional  $\widehat{EA}$ ,  $\widehat{EI}_{xx}$ ,  $\widehat{EI}_{yy}$ , and  $\widehat{EI}_{xy}$  values, as shown in Eqs. (6)–(9). Note that if the bending stiffness or bending moment is calculated about the horizontal axis (*x*-axis or chordwise axis) of the section, it is referred to as *flapwise bending* and is denoted by  $\widehat{EI}_{xx}$ , while if it is calculated about the vertical axis (*y*-axis or the vertical to the chordwise axis) of the section, it is referred to as *edgewise bending* and is denoted by  $\widehat{EI}_{yy}$ 

$$\widehat{EA} = \sum_{i=1}^{n} E_i A_i \tag{6}$$

$$\widehat{EI}_{xx} = \sum_{i=1}^{n} E_i I_{xx,i} \tag{7}$$

$$\widehat{EI}_{yy} = \sum_{i=1}^{n} E_i I_{yy,i} \tag{8}$$

$$\widehat{EI}_{xy} = \sum_{i=1}^{n} E_i I_{xy,i} \tag{9}$$

where  $\widehat{EI}_{xx}$  = effective bending stiffness about the composite centroidal x-axis;  $\widehat{EI}_{yy}$  = effective bending stiffness about the composite centroidal y-axis;  $\widehat{EI}_{xy}$  = effective bending stiffness about the composite centroidal product of x-axis and y-axis;  $\widehat{EA}$  = effective axial stiffness [these stiffnesses are called the "replacement" stiffnesses by Kollar and Springer (2003)];  $E_i$  = Young's modulus ( $E_{x'x'}$ ) of the laminate of the ith part; and n = number of parts composing the cross section.

4. Determine the effective torsional stiffness of the multicellular composite cross section using the method of consistent deformations (Kollar and Springer 2003; Librescu and Song 2005). For a section composed of three cells (i.e., i, j, and k) and by assuming that cell j is the only effective cell in the section, Eq. (10) can be used to determine the rate of twist (θ). However, the assumption is based on zero shear flows in the ith and kth cells. Thus, by correcting this assumption and adding the effect of the ith and kth cells, this will result in Eq. (11). By equating the rate of twists for all the cells to each other since the whole cross section twists as one unit, the shear flows in the cells can be found which can then be used to back calculate the torsional stiffness GJ using Eq. (12)

$$\theta = \frac{T}{\widehat{GJ}} \xrightarrow{\left(T = \sum_{i=1}^{N} 2\Omega_{i}q_{i}\right)} \theta = \frac{q}{2\Omega} \oint \left(\frac{ds}{Gt}\right) \tag{10}$$

$$\theta_{j} = \frac{1}{2\Omega_{j}} \left[ \oint_{s_{j}} q_{j} \left( \frac{ds}{Gt} \right) - \int_{s_{ji}} q_{i} \left( \frac{ds}{Gt} \right) - \int_{s_{jk}} q_{k} \left( \frac{ds}{Gt} \right) \right]$$
(11)

$$\widehat{GJ} = \frac{T}{(1/2\Omega_j) \left[ \oint_{s_j} q_j(ds/Gt) - \int_{s_{jk}} q_i(ds/Gt) - \int_{s_{jk}} q_k(ds/Gt) \right]}$$
(12)

where  $\widehat{GJ}$  = effective torsional stiffness of multicellular cross section; T = applied external torque;  $\theta$  = rate of twist (twist per unit length);  $\Omega$  = enclosed area by a cell; q = shear flow; N = number of cells; G = in-plane shear modulus ( $G_{x'y'}$ ) of the laminate; t = thickness;  $s_j$  = arc length of the jth cell; and  $s_{ii}$  = common arc length of the jth and the ith cells.

A summary of the stiffness distributions along the blade is shown in Fig. 3. As can be seen from Fig. 3(a), the stiffest part that contributes the most to the bending stiffness about the x-axis  $\widehat{EI}_{xx}$  is the spar caps, while in Fig. 3(b), the stiffest part contributing the most about the y-axis  $\widehat{EI}_{yy}$  is the shell. Note that the distribution of the bending stiffness for the product moment of inertia [Fig. 3(c)] has relatively small values for most of the stations indicating that the principal directions of the cross sections are relatively close to the flapwise and edgewise bending directions (i.e.,  $\widehat{EI}_{xx}$  and  $\widehat{EI}_{yy}$ , respectively). The axial stiffness is affected by both the shell and the spar caps [Fig. 3(d)]. The torsional stiffness shown in Fig. 3(e) is based on the overall cross-sectional properties (hence it is shown in one color only); since the cells are composed of different parts of the spar, shell, and webs, it is not possible to attribute the effective  $\widehat{GJ}$  to any of these parts separately (for example, the middle cell is composed of the spar caps and the two webs and the webs are also part of the leading edge and trailing edge cells) like the effective  $\widehat{EA}$  and  $\widehat{EI}$ s. Therefore, the  $\widehat{GJ}$  is shown for the entire section as a function of length.

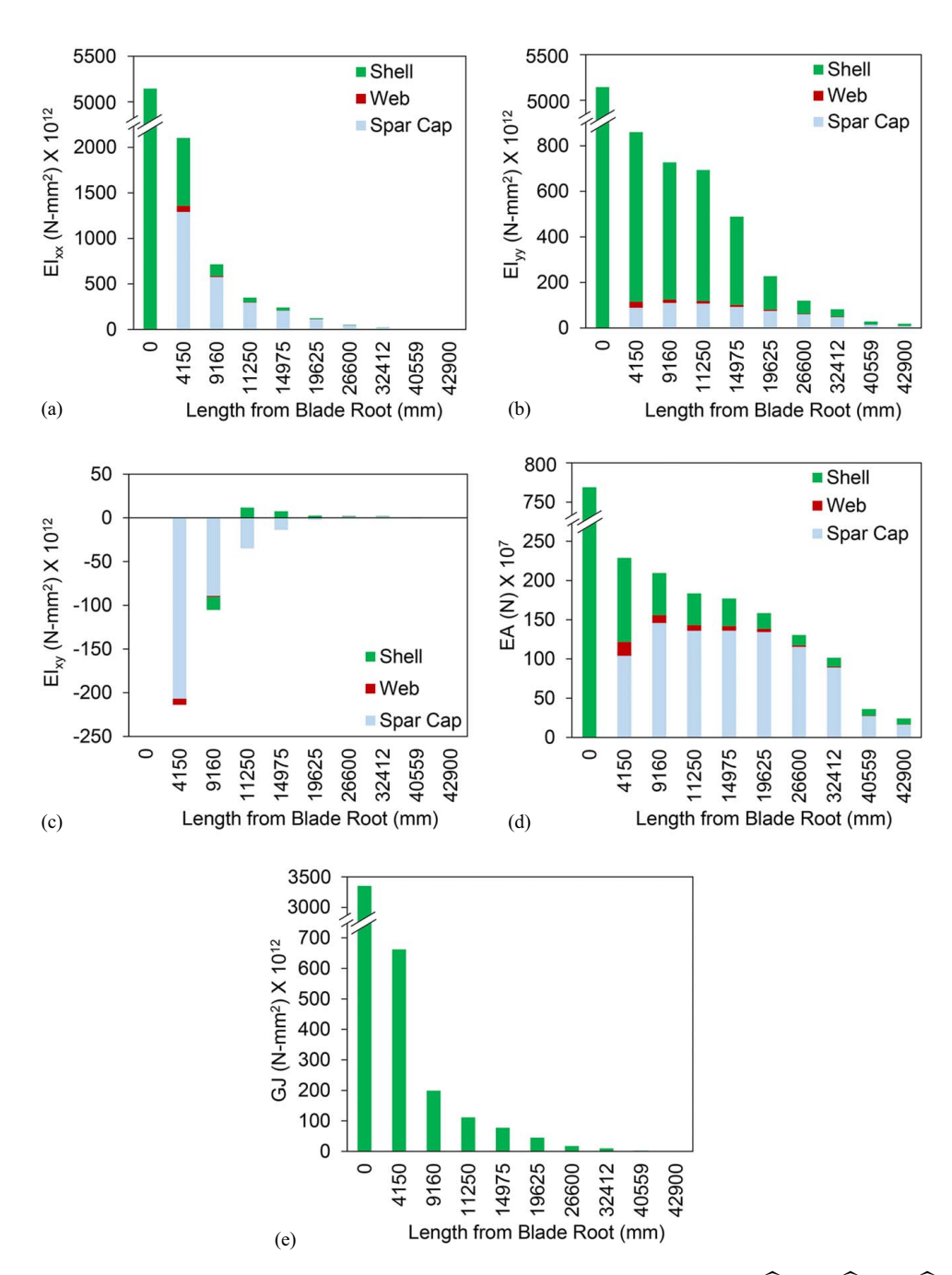


Fig. 3. Stiffness distribution in the three primary substructures: the shell, the spar caps, and the webs for (a)  $\widehat{EI}_{xx}$ ; (b)  $\widehat{EI}_{yy}$ ; (c)  $\widehat{EI}_{xy}$ ; (d)  $\widehat{EA}$ ; and (e)  $\widehat{GJ}$ .

## **Details of the Proposed Electrial Transmission Pole**

The research team is currently working on developing various configurations of the wind blade as electrical transmission and distribution poles ranging from 20 to 45 m in height. Fig. 4 shows the most basic configuration, in which the three phases (with likely voltages of 69 or 138 kV for the North American electrical grid) and their conductors (the electric wires) are connected to the wind blade structure through special FRP molded crossarms which are securely bolted to the spar cap material. The proposed structure represents a single 20.6 m long part of the C96 blade cut from the tip as a tangent pole with 7.0 m long crossarms in which each crossarm extends 3.5 m from the center of the pole either to the left or to the right. (If six phases are needed, a longer segment of the blade is needed, and different structural analysis is required). However, it is important to note that the current configuration has a large

bending moment at the upper crossarm due to the nonsymmetric phase distribution, while the case of six phases will be symmetric resulting in lower eccentricity and bending stresses. The wind blade is connected to the ground with a concrete pier foundation with steel rebar extending into the blade's cavity, which is filled with concrete grout. The existing copper lightning conductor shown in Fig. 2 is employed as the grounding cable.

## Structural Analysis of the BladePole

ASCE Manual of Practice 74 (Wong and Miller 2009) and NESC (IEEE 2017) are the standards usually followed in the design of electrical transmission structures in the United States. They give detailed descriptions and derivations of the different load cases that need to be applied to such structures. These load cases may involve (1) extreme

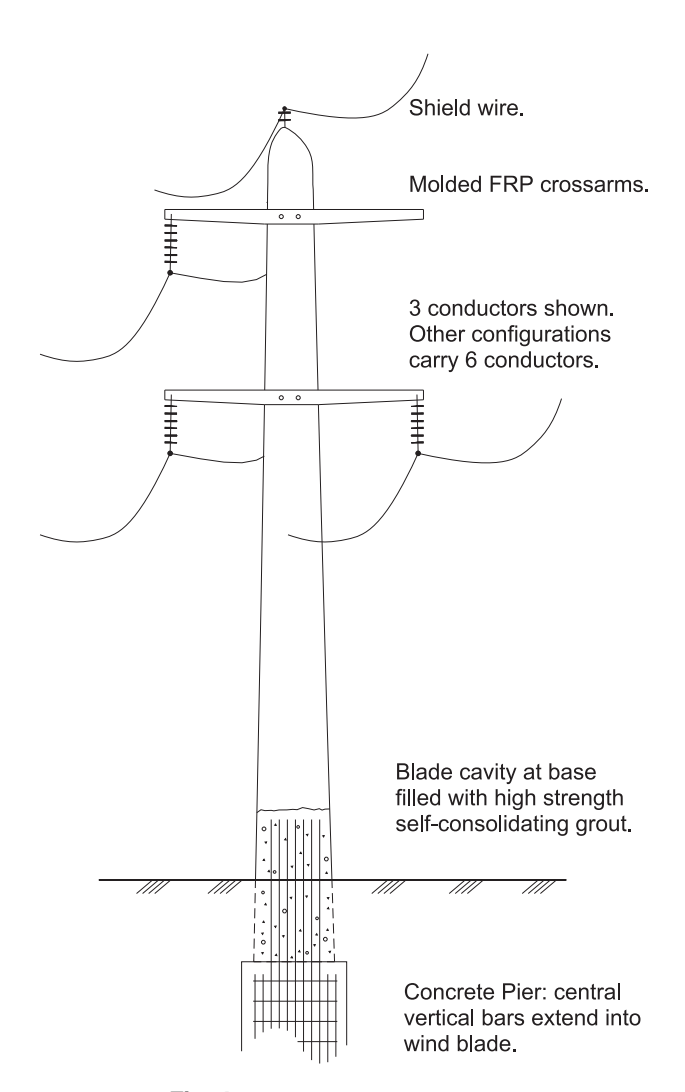


**Fig. 4.** BladePole concept proposal.

wind; (2) combined wind and ice; (3) extreme ice; (4) differential ice; (5) broken conductor; and (6) broken shield wire.

In the current study, in addition to these load cases, the shape of the wind blade combined with the direction of the wind on the blade creates additional load cases at different angles (i.e.,  $0^{\circ}$ ,  $45^{\circ}$ ,  $135^{\circ}$ ,  $180^{\circ}$ ,  $225^{\circ}$ , and  $315^{\circ}$ ). This resulted in a total of 16 load cases that were reduced into eight key load cases that are presented here, as follows:

- 1. extreme wind of 144.8 km/h (90 mph) at 0°,
- 2. extreme wind of 144.8 km/h (90 mph) at 90°.
- 3. extreme wind of 144.8 km/h (90 mph) at 45°,
- 4. concurrent wind of 48.3 km/h (30 mph) at 0° and ice of 19.1 mm.
- 5. extreme ice of 25.4 mm formed on the conductors,
- 6. differential ice of 24.5 mm on one side and 12.7 mm on the other side.
- 7. broken conductor (any), and
- 8. broken shield wire (any).

Table 3 and Fig. 5 show the details of the eight load cases following the configuration proposed for the BladePole in Fig. 4. Note that P is the axial force, V is the shear force, M is the bending moment, and T is the torsional moment.

After the cross-sectional stiffnesses and load cases have been determined, the structural model of the pole is developed. Fig. 6 shows the simplified structural model of the BladePole. The BladePole is modeled as a space frame using 1D beam elements. It is

Table 3. Load cases details

	For	rce (N)	Wind pre	Wind pressure (Pa)		
Case No.	Vertical	Horizontal	0 deg	90 deg		
1	1,779 <sup>a</sup> 12,455 <sup>b</sup>	0	1,005	0		
2	1,779 <sup>a</sup> 12,455 <sup>b</sup>	0	0	1,005		
3	1,779 <sup>a</sup> 12,455 <sup>b</sup>	0	718	718		
4	7,117 <sup>a</sup> 31,138 <sup>b</sup>	0	96	0		
5	4,448 <sup>a</sup> 23,131 <sup>b</sup>	0	0	0		
6	3,559 <sup>a</sup> 20,017 <sup>b</sup>	0	0	0		
7	1,779 <sup>a</sup> 12,455 <sup>b</sup> 3,559 <sup>c</sup>	-7,117 <sup>a</sup> 10,676 <sup>c</sup>	0	0		
8	1,779 <sup>a</sup> 12,455 <sup>b</sup> 445 <sup>d</sup>	5,338 <sup>d</sup>	0	0		

<sup>&</sup>lt;sup>a</sup>Load per shield wire.

fixed at the base and free at the top in the x–z plane. It is fixed at the base and restrained at the top in the y–z plane by the effect of the conductors and shield wires for poles installed in a tangent configuration where the pretensioned cables reduce the longitudinal movement at the top of the poles. The insulators that are connected to the crossarms, davits, or braced line posts are permitted only a small longitudinal movement due to uneven loads on different cable spans. Using the loads and effective stiffnesses at each station described previously, a structural frame analysis using Visual Analysis (IES 2019) and Mastan2 (McGuire et al. 2000) with user-defined cross-sectional properties was conducted.

The load case that controls the bending and axial loading is *Concurrent Ice and Wind* (Load Case 4), while the load case that controls the shear loading is *Extreme Wind* (Load Case 2). The load case that controls the torsional loading is *Broken Conductor* (Load Case 7). The resulting axial force, shear force, and bending and torsional moment diagrams for Load Cases 4, 2, and 7 are shown in Figs. 7(a–c), respectively.

Axial stresses [using Eq. (13)], shear flows [using Eq. (14)] due to bending, and shear flows due to torsion [using Eq. (15)] are then obtained. The axial and shear stress distributions (i.e., the shear flows multiplied by the thicknesses) for the three controlling load cases (4, 2, and 7) along the height of the BladePole are then obtained (Oden and Ripperger 1981). [Note that Eqs. (14) and (15) are based on transformed and segmented cross sections in which the cross section is divided into straight segments and then these segments are transformed based on the lowest modulus of elasticity of the cross section.]

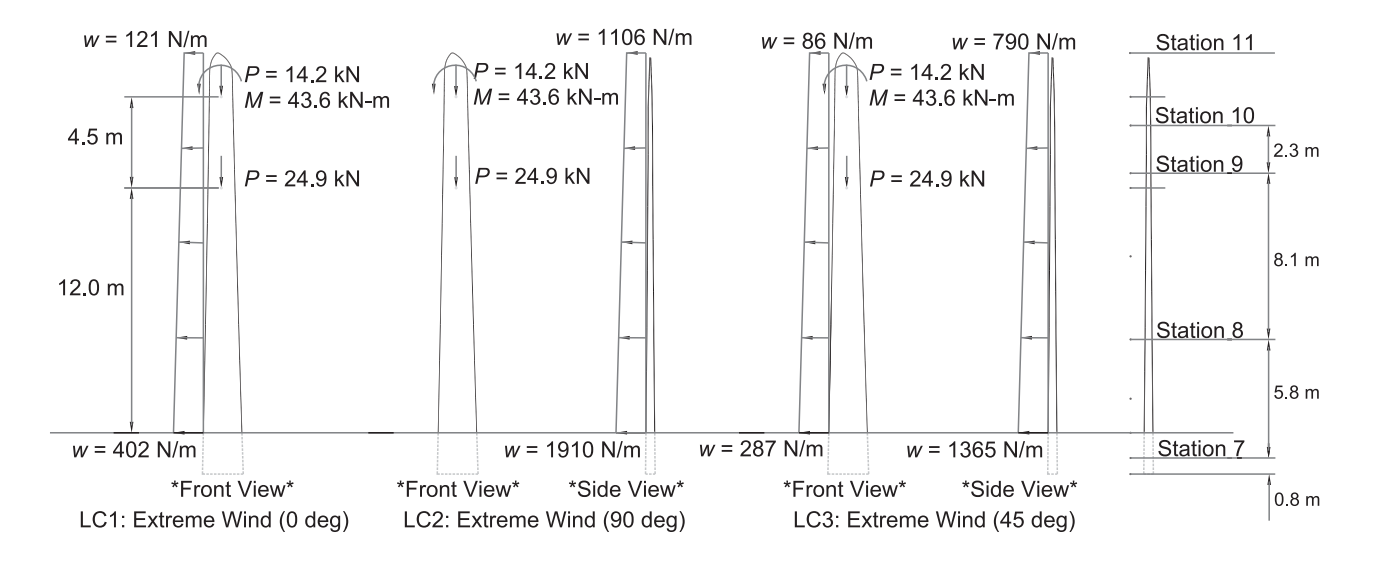
$$\sigma_{z} = \frac{PE_{i}}{\widehat{EA}} + E_{i} \left( \frac{M_{x}\widehat{E}I_{yy} - M_{y}\widehat{E}I_{xy}}{\widehat{E}I_{xx}\widehat{E}I_{yy} - \widehat{E}I_{xy}^{2}} \right) y - E_{i} \left( \frac{M_{y}\widehat{E}I_{xx} - M_{x}\widehat{E}I_{xy}}{\widehat{E}I_{xx}\widehat{E}I_{yy} - \widehat{E}I_{xy}^{2}} \right) x$$

$$(13)$$

bLoad per phase.

<sup>&</sup>lt;sup>c</sup>Load per phase carrying the broken conductor.

<sup>&</sup>lt;sup>d</sup>Load per the broken shield wire.



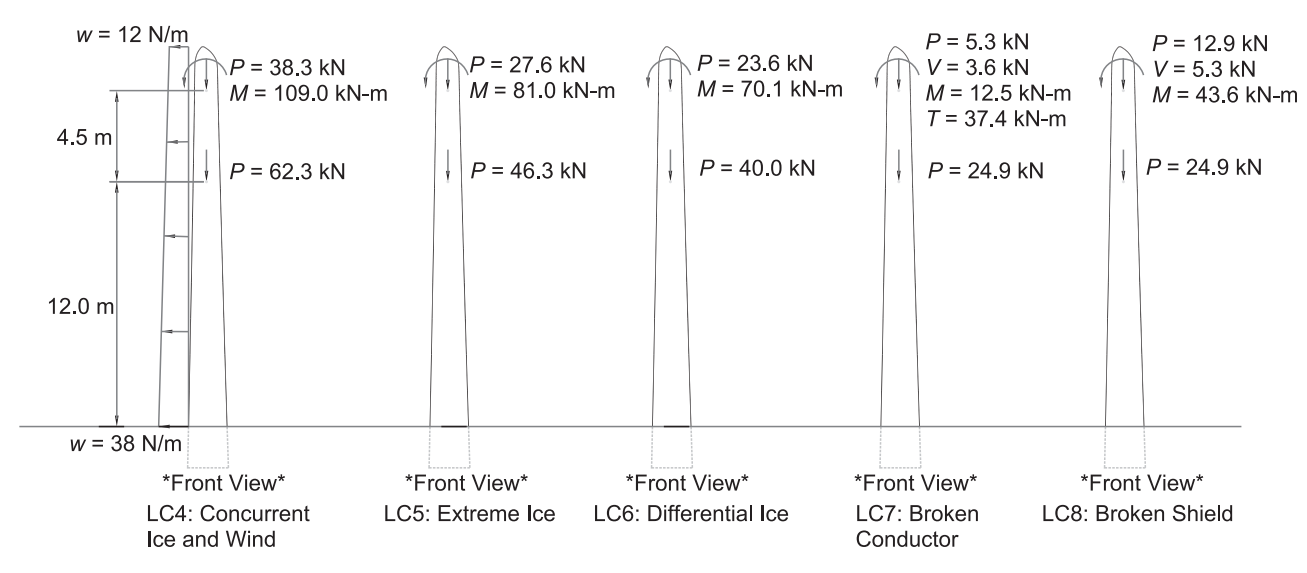


**Fig. 5.** Load cases for the BladePole.

$$q = \left(\frac{Q_x I_{yy} - Q_y I_{xy}}{I_{xx} I_{yy} - I_{xy}^2}\right) V_y + \left(\frac{Q_y I_{xx} - Q_x I_{xy}}{I_{xx} I_{yy} - I_{xy}^2}\right) V_x \tag{14}$$

$$q = \frac{2T\Omega}{\widehat{GJ} \oint (ds/Gt)}$$
 (15)

where  $\sigma_z$  = axial stress from both axial force and bending moment;  $M_x$  = applied external flapwise bending moment (moment about the x-axis of the cross section);  $M_y$  = applied external edgewise bending moment (moment about the y-axis of the cross section); P = applied external axial load (+ve means tension); x and y = coordinates of the point where stress to be determined with respect to the composite centroid,  $Q_x$  = first moment of area about the centroidal x-axis;  $Q_y$  = first moment of area about the centroidal y-axis;  $V_x$  = shear force in the x-axis (the flapwise direction); and  $V_y$  = shear force in the y-axis (the edgewise direction).

Fig. 8(a) shows the axial stresses generated in the pole due to axial forces and bending moments resulting from Load Case 4. The stress and strain distributions across the depth of the cross section at Stations 7, 8, 9, and 10 are shown in Figs. 8(b—e), respectively. It is noteworthy to mention that for the axial tensile stresses, the spar cap attracts more stresses than the shell even though the

shell is the furthest from the composite centroid of the cross section; this is because the spar cap material is the stiffest. However, this is not the case for the axial compressive stresses due to the large distance of the trailing edge material from the composite centroid (see Fig. 1). The results reveal that the maximum compressive stresses at Station 10 (the critical station) were 71.7, 66.0, and 24.1 MPa for the shell, the spar caps, and the webs, respectively, while the maximum tensile stresses were 49.7, 69.1, and 25.2 MPa for the shell, the spar caps, and the webs, respectively.

Fig. 9(a) shows the shear stress distribution with the height of the BladePole for Load Case 2 (the case with the highest shear forces). Figs. 9(b and c) show the shear flows and shear stresses at the critical station (i.e., Station 7) resulting from torsional moments and shear forces, respectively. Fig. 9(d) shows the combined shear flows and shear stresses from torsion and shear at Station 7 in which the critical locations in the cross section (where maximum shear stresses occur) are highlighted (with circles).

Fig. 10(a) shows the shear stresses along the height of the Blade-Pole for Load Case 7, while Figs. 10(b–e) show the shear flows and shear stresses resulting from torsional moments at Stations 7, 8, 9, and 10, respectively. Note that the shear flows and shear stresses from torsion are constant across the single material (i.e., the leading edge, the trailing edge, the upper spar cap, the lower spar cap, the

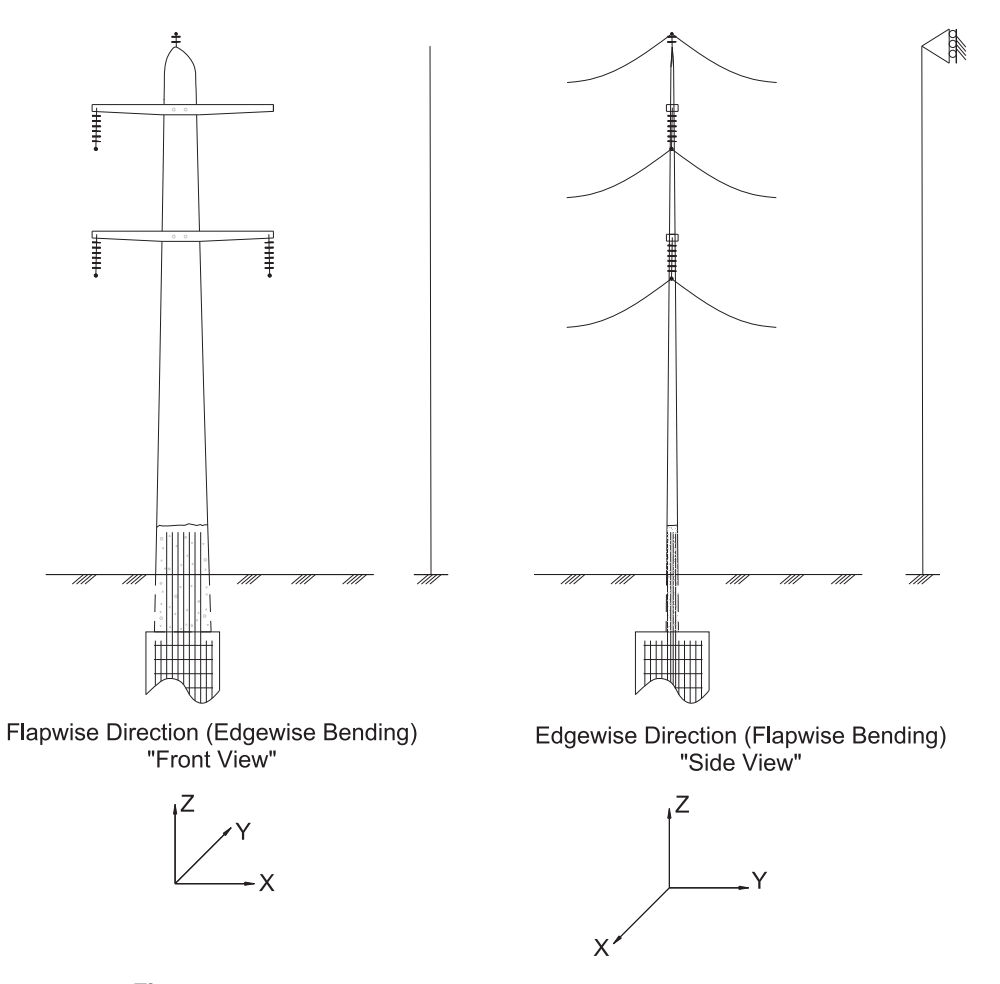


Fig. 6. Simplified model used in the structural analysis of the BladePole

front web, and the rear web), which is different than the case of shear flows from shear forces. It is interesting to note that the spar caps attract the highest shear flows due to their large thickness even though their shear stiffnesses are the lowest, and consequently, these large shear flows are converted to small shear stresses due to these large thicknesses. On the contrary, even though the webs have the lowest thicknesses, they attract the highest stresses due to their high shear moduli and low thicknesses. As in Fig. 9, critical stresses are identified by circles on the diagram.

#### **Deflections of the BladePole**

In many cases, FRP composite structures are governed by serviceability limit states (SLS) rather than ultimate limit states (ULS) due to their high strength to stiffness ratios (Bank 2006). Figs. 11(a and b) show the expected axial shortening and horizontal drift of the BladePole under compressive loads and bending moments, respectively. As can be seen, the axial deformation is negligible, however, the horizontal drift needs to be checked against governing serviceability limit states for electrical power transmission structures. Guidance on the serviceability limits can be found in the ASCE Manual of Practice 104 (Task Committee on Fiber-Reinforced Polymer Products for Overhead Utility Line Structures 2019). Even though there are no specific limits due to the novel nature of FRP poles, recommendations of a limit of around 8%-15% of the aboveground height (AGH) of the pole are typical. Since the aboveground height of the pole is 18.6 m, a conservative drift limit of 8% results in an allowable horizontal tip displacement of 1,490 mm. Fig. 11(b) shows a maximum value of 344 mm proving that the pole conforms to the deflection serviceability limit states. The natural frequency SLS will need to be checked in future work.

Additionally, shear deflections can be of interest for cases where shear loads are large; thus, the effect of combined shear and bending deflection for load cases where shear loads are present are compared to bending-only deflections and shown in Fig. 12. It is important to mention that the deflections shown in Fig. 12 are for the y-direction where there is a roller support at the top of the pole and zero deflection. The figures were drawn with the simplifying assumptions that only the spar cap material resists any shear forces in the x-axis (flapwise direction) and only the web material resists any shear forces in the y-axis (edgewise direction). As it can be seen from Figs. 12(a and b), the effect of combining the shear deflection results in a maximum increase of 12.4% in deflection, while Fig. 12(c) shows a maximum increase of 19.8% proving that the effects of shear deformations should be accounted for in serviceability checks of wind blades used in this application. Nevertheless, drift limits do not control the current design.

## **Results of Stress Analysis**

A complete summary of the expected maximum compressive, tensile, and shear stresses in all parts alongside deflection values for all load cases is shown in Table 4. For comparison purposes, Helius Composite (Autodesk 2016) was used to obtain theoretical values for the strengths and stiffnesses of the composites in the different

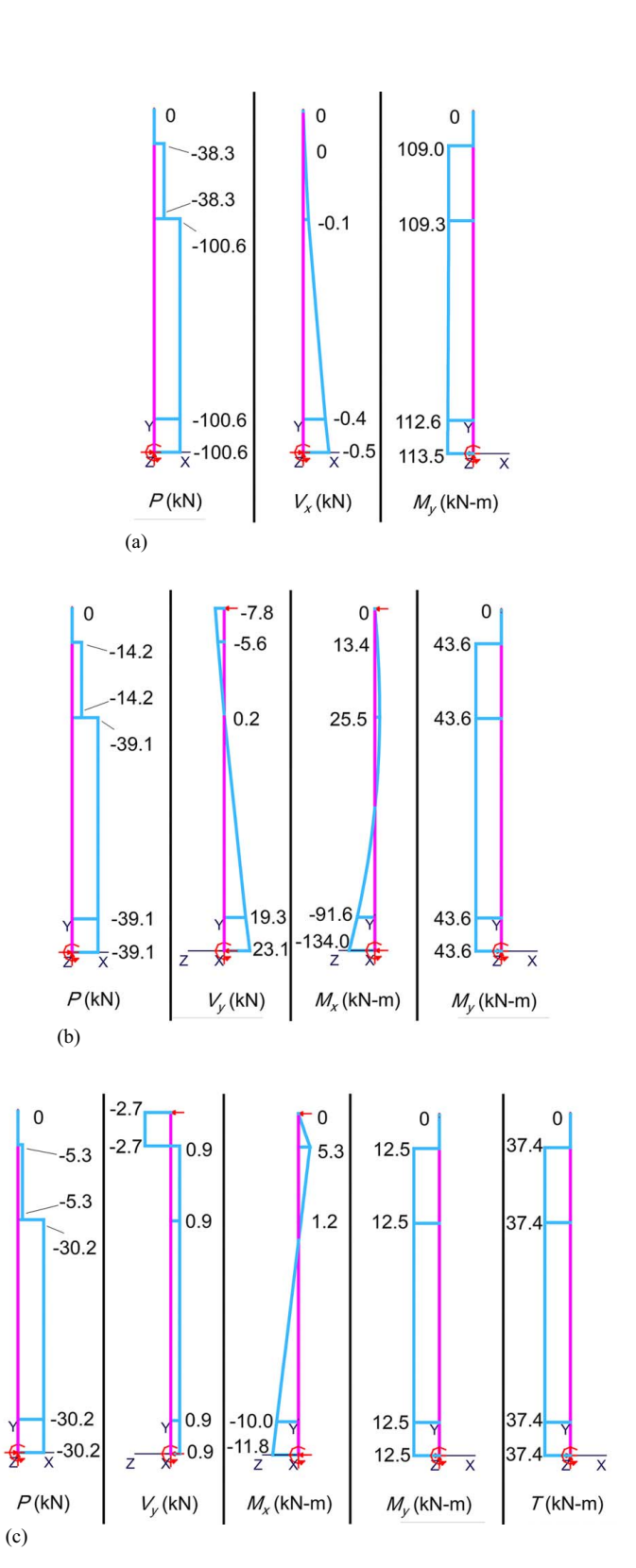


**Fig. 7.** Axial, shear, bending, and torsional moment diagrams for the controlling load cases: (a) Case 4; (b) Case 2; and (c) Case 7.

parts (i.e., the shell, the spar caps, and the webs). These values are given in Table 5. In addition, data from the OPTIDAT database is given in Table 6 (Nijssen et al. 2007), in which the results for testing of uniaxial, biaxial, and triaxial glass fiber composites are presented. This approximates, to an acceptable degree, the composites in the spar caps (mostly uniaxial), in the webs (biaxial), and the shell (triaxial). It is important to note that the strength and modulus

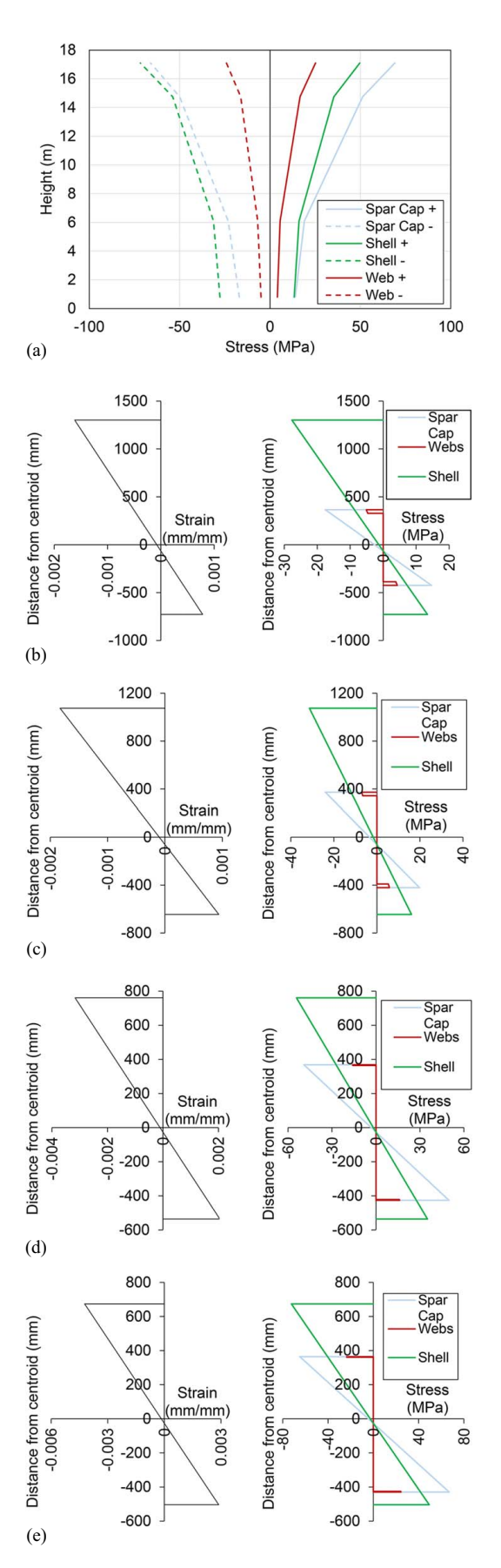


**Fig. 8.** Load Case 4 stresses: (a) axial stresses at all stations; (b) stresses and strains at Station 7; (c) stresses and strains at Station 8; (d) stresses and strains at Station 9; and (e) stresses and strains at Station 10.

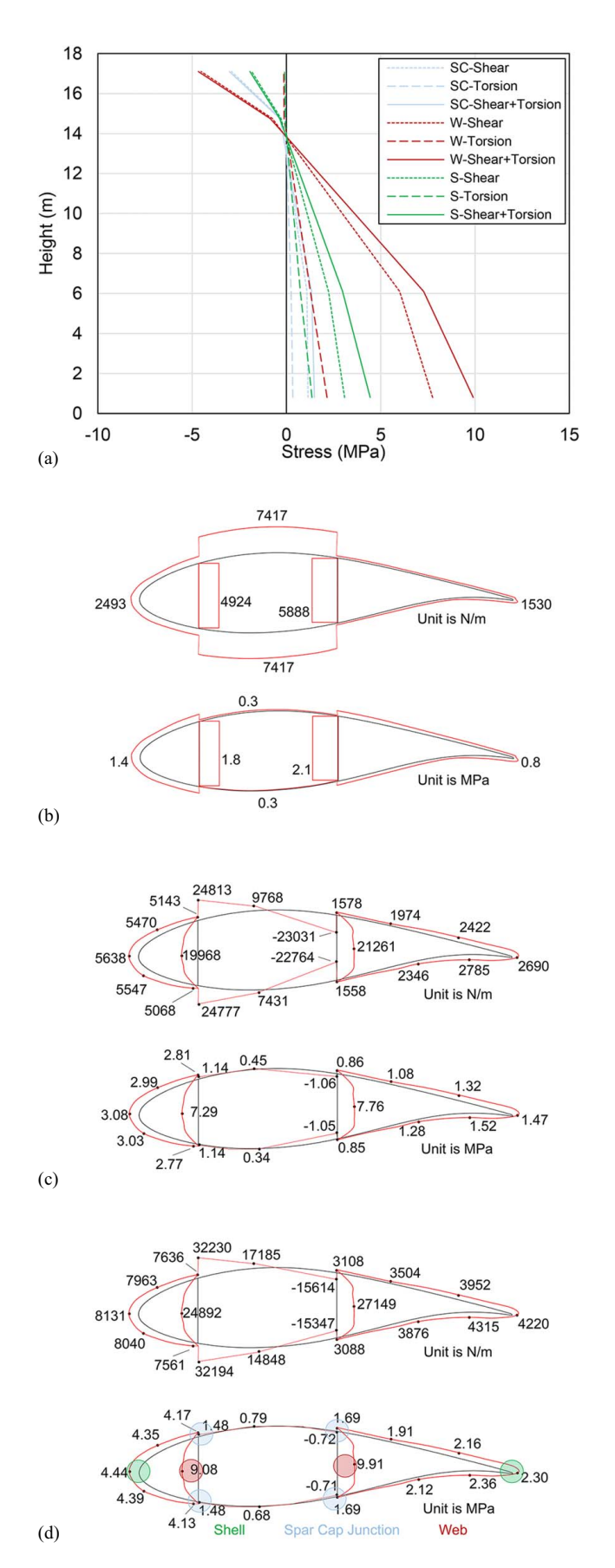


**Fig. 9.** Load Case 2 stresses: (a) shear stresses along the pole at all stations; (b) shear stresses and flows from torsion only at Station 7; (c) shear stresses and flows from shear loads only at Station 7; and (d) shear stresses and flows from both shear loads and torsion at Station 7.

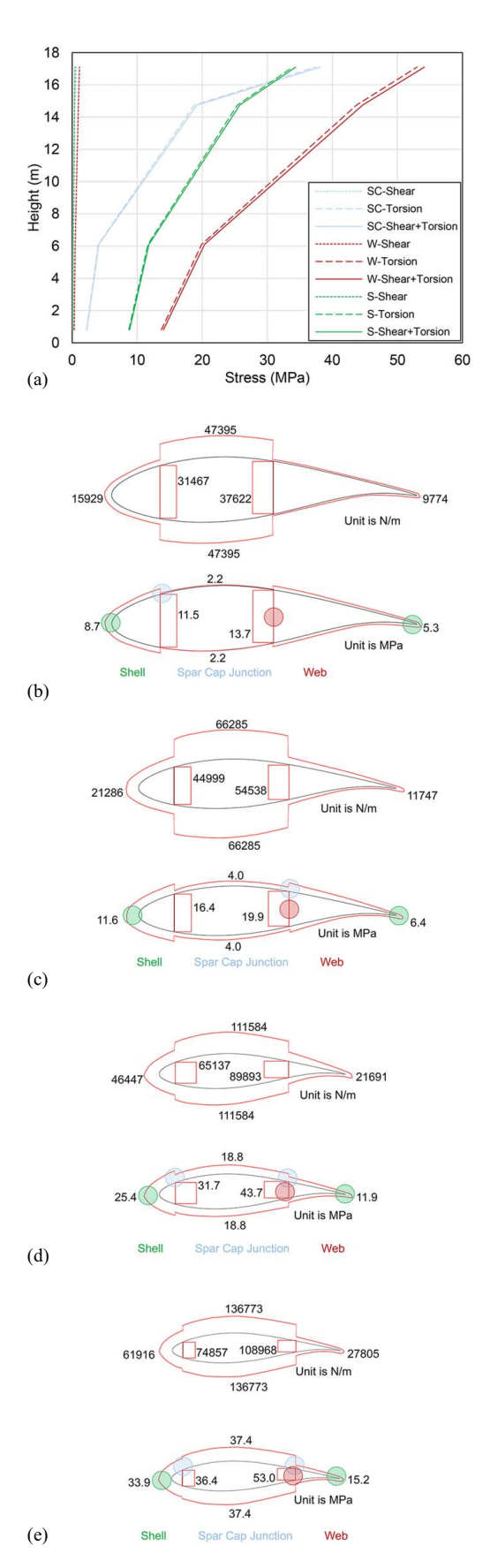


**Fig. 10.** Load Case 7 stresses: (a) shear stresses along the pole at all stations; (b) shear stresses and flows from torsion at Station 7; (c) shear stresses and flows from torsion at Station 8; (d) shear stresses and flows from torsion at Station 9; and (e) shear stresses and flows from torsion at Station 10.

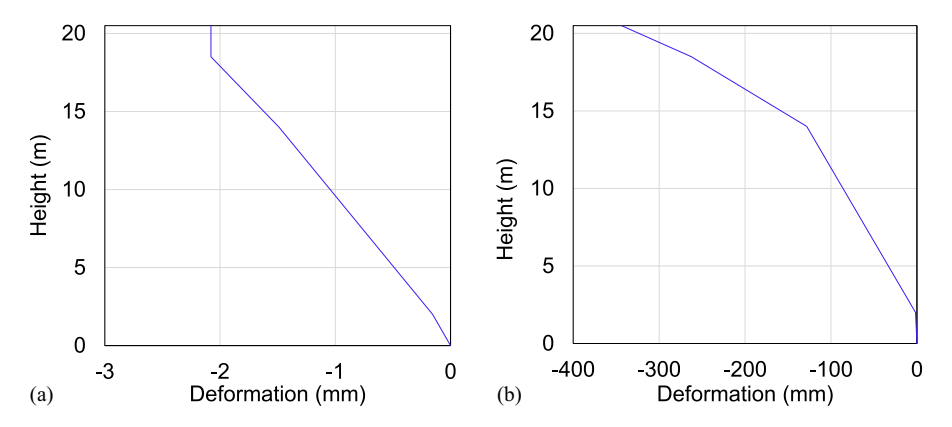
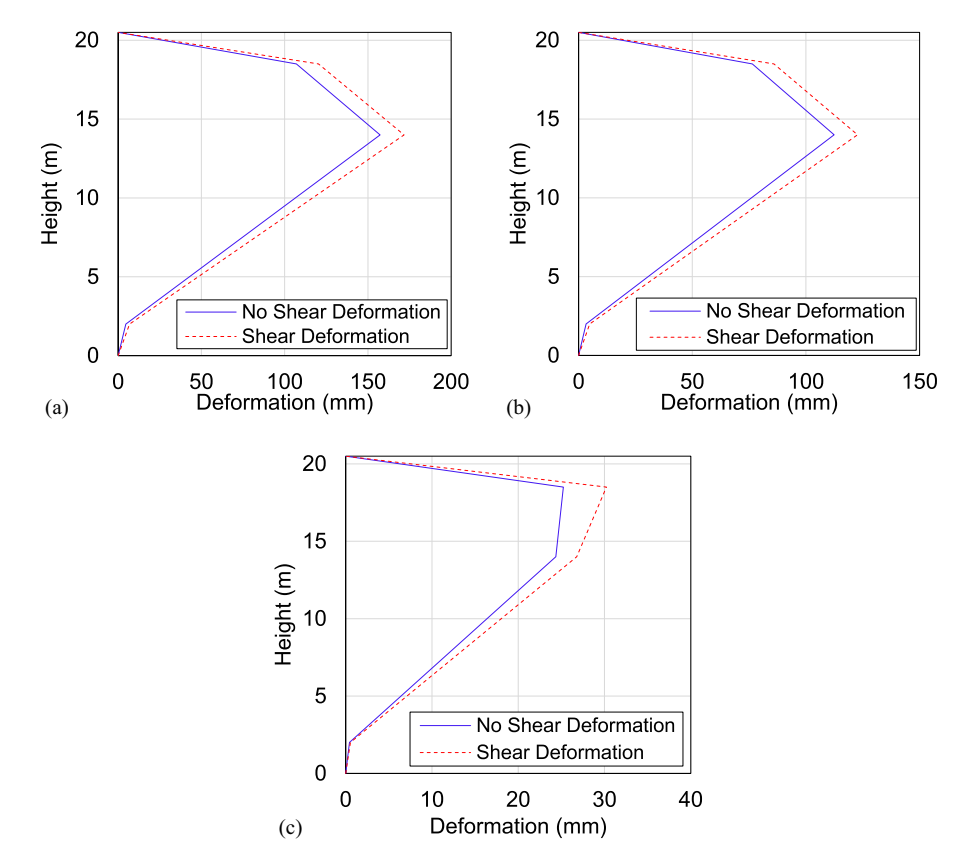


Fig. 11. Deflection from Load Case 4 for (a) axial z-direction; and (b) horizontal x-direction.



**Fig. 12.** Values of shear deformation with respect to bending deformations in the *y*-direction for (a) Load Case 2; (b) Load Case 3; and (c) Load Case 7.

data presented herein are for wind blades that are newly manufactured. Trends in the data from the literature showed that a slight decline (10%–20%) in the strength and stiffness is observed in the life of fatigued composite materials (forming the wind blades), while a sudden drop is attained near their full design life (Post 2005; Nijssen 2006; Post et al. 2008). Materials testing and full-scale structural testing is being conducted on used wind blades by the research team to validate these findings for wind blade composites.

For the case of controlling axial stresses (i.e., Load Case 4), maximum tensile stresses in the shell, the spar caps, and the webs are 49.7, 69.1, and 25.2 MPa, respectively, and the maximum compressive stresses are 71.7, 66.0, and 24.1 MPa, respectively. If compared with the data from the OPTIDAT database (experimental results) and Helius Composite (theoretical results based on progressive failure analysis), a minimum safety factor of 2.8 is obtained for

the shell materials. It is important to note that the 3.5 m crossarm extension is assumed for the current proposed configuration; however, the length used in the field may be less, which will result in lower bending moment values that will increase the safety margin even further. It is important to note that experimental validation of fatigued wind blade material properties might reduce this factor. This reduction of mechanical properties due to prior use is an ongoing topic of investigation by this research team.

For the controlling shear stresses cases (i.e., Load Case 2 and Load Case 7), the maximum shear stresses in the shell, the spar caps, and the webs are 34.4, 38.1, and 54.1 MPa, respectively. If compared with the given data, a minimum safety factor of 1.9 is obtained for the spar cap materials. Even though this factor might be considered low for civil engineering infrastructure, it is important to note that the case resulting in this value (i.e., Load

Table 4. Summary of maximum stresses and deflections for all cases and all substructures

Maximum tensile stress (MPa)		Maximum compressive stress (MPa)		Maximum shear stress (MPa)			Maximum deflection (mm)					
Case No.	Shell	Web	Spar cap	Shell	Web	Spar cap	Shell	Web	Spar cap	x	у	z
1	20.5	10.4	28.5	-29.3	-9.8	-26.9	0.8	0.2	0.2	-188.5	0.0	-0.8
2	28.1	14.1	45.2	-30.1	-12.4	-36.7	4.4	9.9	3.0	-135.5	157.3	-0.8
3	22.6	13.0	36.4	-30.2	-11.6	-31.8	3.7	7.1	2.1	-173.4	112.4	-0.8
4	49.7	25.2	69.1	-71.7	-24.1	-66.0	0.1	0.0	0.0	-343.8	0.0	-2.1
5	36.9	18.7	51.3	-53.1	-17.8	-48.9	0.0	0.0	0.0	-251.7	0.0	-1.5
6	32.0	16.2	44.5	-45.9	-15.4	-42.3	0.0	0.0	0.0	-217.9	0.0	-1.3
7	6.8	3.7	10.9	-8.7	-3.4	-9.4	34.4	54.1	38.1	-38.9	25.2	-0.5
8	19.1	11.1	30.4	-28.9	-10.2	-27.9	0.8	1.9	1.2	-135.5	37.2	-0.8

**Table 5.** Summary of theoretical values for compressive strength and stiffness of different parts at Station 10 (42,900 mm from the root)

Part	Layup of the laminate	$E_{x'x'}$ (MPa)	$F_t^0$ (MPa)	$F_c^0$ (MPa)	F <sub>v</sub> (MPa)
Shell	[±45/0/±45]	17,130	271.65	197.67	144.93
Spar	$[(\pm 45)_2/0_8/$	27,548	673.07	453.47	72.74
cap	$(\pm 45)_2$ ]				
Web	[±45]	10,048	145.62	145.62	193.05

Note:  $E_{x'x'}$  = longitudinal Young's modulus;  $F_t^0$  = longitudinal tensile strength;  $F_c^0$  = longitudinal compressive strength; and  $F_v$  = shear strength.

Table 6. Representative material properties from the OPTIDAT database

Material	$E_{x'x'}$ (MPa)	$E_{y'y'}$ (MPa)	<i>G</i> <sub>x'y'</sub> (MPa)	$ u_{x'y'}$	ρ (kg/ m <sup>3</sup> )	$F_t^0$ (MPa)	$F_c^0$ (MPa)
Uniaxial	38,887	9,000	3,600	0.249	1,869	810	507
Triaxial	24,800	11,500	4,861	0.416	1,826	436	349
Biaxial	11,700	11,700	9,770	0.501	1,782	180	144

Source: Adapted from Nijssen et al. (2007).

Note:  $E_{x'x'}$  = longitudinal Young's modulus;  $E_{y'y'}$  = transverse Young's modulus;  $G_{x'y'}$  = in-plane shear modulus;  $\nu_{x'y'}$  = in-plane major Poisson's ratio;  $\rho$  = density;  $F_t^0$  = longitudinal tensile strength; and  $F_c^0$  = longitudinal compressive strength.

Case 7) is a sudden breakage in the conductor and the modeling of the pole did not employ the restraining effect of the other conductors to the blade pole structure, which may increase the safety margins by partial restraint and reduction of the torsional moments on the pole.

#### **Conclusions**

Repurposing of decommissioned wind turbine blades at the end of their first life is necessary to prove their long-term sustainable nature. This paper presents a preliminary assessment and feasibility study for the repurposing of a decommissioned wind turbine blade as a vertically cantilevering single electrical pole called a BladePole. The following findings are emphasized:

- A proposed configuration for a basic power pole has been analyzed, designed, and detailed. In order to be commercialized, it will need to be approved for various types of wind blades and electrical transmission structures in various configurations (e.g., three or six phases) and for service in different environments. This will require full-scale testing and qualifying proof tests.
- Governing load cases and combinations from ASCE and NESC standards proved the adequacy of the wind blade materials to resist the expected structural loads with reasonable safety

margins. Even though there are some recommendations for the design of FRP power poles, only manuals of practice exist regarding these materials. Thus, this study is intended to obtain introductory safety margins that will lead to the development of probability-based strength reduction factors.

- Simplified frame analysis using 1D beam elements is possible for wind turbine blades used as structural members. However, detailed 3D finite-element analysis (FEA) may need to be conducted to investigate local regions of high stress concentrations at junctions of the blade parts. The research team has previously discussed the use of a 3D FEA for a roof structure designed from a section of a wind turbine blade and is currently working on the BladePole FEA analysis.
- Stress distributions across the different subcomponents at controlling stations highlight possible failure locations and will lead to the development of specific crossarm and footing connection types that guarantee appropriate stress transfer.
- Preliminary findings of this work are intended to lay the groundwork for future structural reliability-based design guidelines of the proposed BladePole. The stress factors demonstrate that the design and therefore the concept is feasible from the structural point of view. However, the overall reliability index (β) cannot be calculated at this time as the probability distribution functions for the loads, the materials, and the structural models have not been derived. Therefore, future work will include:
- Design variations that work to reduce torsional stresses.
- Material evaluation to establish the mean and scatter expected in material properties.
- 3D finite-element analysis to validate the stresses and deflections from the 1D analysis.
- Structural reliability models to establish strength reduction factors for design guidelines.

## **Data Availability Statement**

All data, models, or codes that support the findings of this study are available from the corresponding author upon reasonable request.

#### **Acknowledgments**

Support for this research was provided by the National Science Foundation (NSF) under grants 1701413 and 1701694; by InvestNI/Department for the Economy (DfE) under grant 16/US/3334 and by Science Foundation Ireland (SFI) under grant USI-116 as part of the US-Ireland Tripartite research program.

#### References

- Alshannaq, A., D. Scott, L. Bank, M. Bermek, and R. Gentry. 2019. "Structural re-use of de-commissioned wind turbine blades in civil engineering applications." In *Proc.*, 34th Technical Conf. of the American Society for Composites, 14. Lancaster, PA: DEStech. https://doi.org/10.12783/asc34/31317.
- ASTM. 2018. Standard test method for ignition loss of cured reinforced resins. ASTM D2584. West Conshohocken, PA: ASTM.
- Autodesk. 2016. "Autodesk Helius composite. V. 2016." Accessed January 1, 2020. https://www.autodesk.com/products/helius-composite/overview.
- Autodesk. 2019. "Autodesk AutoCAD. V. 2019." Accessed January 1, 2020. https://www.autodesk.com/products/autocad/overview.
- Bank, L., et al. 2018a. "Re-wind design atlas." Accessed August 1, 2020. https://www.re-wind.info/product/2020/8/5/re-wind-releases-its-design -atlas-creative-commons-license-cc-by-nc-sa-40.
- Bank, L. C. 2006. Composites for construction: Structural design with FRP materials. Hoboken, NJ: Wiley.
- Bank, L. C., F. R. Arias, A. Yazdanbakhsh, T. R. Gentry, T. Al-Haddad, J.-F. Chen, and R. Morrow. 2018b. "Concepts for reusing composite materials from decommissioned wind turbine blades in affordable housing." *Recycling* 3 (1): 3. https://doi.org/10.3390/recycling3010003.
- Brøndsted, P., H. Lilholt, and A. Lystrup. 2005. "Composite materials for wind power turbine blades." *Annu. Rev. Mater. Res.* 35 (1): 505–538. https://doi.org/10.1146/annurev.matsci.35.100303.110641.
- Gentry, R., T. Al-Haddad, L. C. Bank, F. R. Arias, A. Nagle, and P. Leahy. 2020. "Structural analysis of a roof extracted from a wind turbine blade." *J. Arch. Eng.* 26 (4): 04020040. https://doi.org/10.1061/(ASCE)AE.1943-5568.0000440.
- Gentry, R., L. C. Bank, J. F. Chen, F. Arias, and T. Al-Haddad. 2018. "Adaptive reuse of FRP composite wind turbine blades for civil infrastructure construction." In *Proc., 9th Int. Conf. on Fiber Reinforced Polymer Composites in Civil Engineering*, 692–698. Paris: IIFC. Accessed April 15, 2021. http://www.iifc.org/wp-content/uploads/2010/06/CICE2018\_Proceeding\_Part1.pdf.
- Hayman, B., J. Wedel-Heinen, and P. Brøndsted. 2008. "Materials challenges in present and future wind energy." MRS Bull. 33 (4): 343–353. https://doi.org/10.1557/mrs2008.70.
- IEEE (Institute of Electrical and Electronics Engineers). 2017. National electrical safety code. New York: IEEE.
- IES (Integrated Engineering Software). 2019. "IES visual analysis. V. 2019." Accessed January 1, 2020. https://www.iesweb.com/ya/index.html.
- Katnam, K. B., A. J. Comer, D. Roy, L. F. M. da Silva, and T. M. Young. 2015. "Composite repair in wind turbine blades: An overview." *J. Adhes.* 91 (1–2): 113–139. https://doi.org/10.1080/00218464.2014.900449.
- Kollar, L. P., and G. S. Springer. 2003. Mechanics of composite structures. New York: Cambridge University Press.
- Librescu, L., and O. Song. 2005. Thin-walled composite beams: Theory and application. Dordrecht, Netherlands: Springer.

- Liu, P., and C. Y. Barlow. 2017. "Wind turbine blade waste in 2050." Waste Manage. (Oxford) 62: 229–240. https://doi.org/10.1016/j .wasman.2017.02.007.
- Matweb. 2020. "Technical data of E-glass fiber." Accessed January 1, 2020. http://www.matweb.com/search/DataSheet.aspx?MatGUID=d9c 18047c49147a2a7c0b0bb1743e812&ckck=1.
- McGuire, W., R. H. Gallagher, and R. D. Ziemian. 2000. *Matrix structural analysis*. New York: Wiley.
- Metyx Composites. 2020. "Technical datasheet of RIMR 135." Accessed January 1, 2020. https://www.metyx.com/wp-content/uploads/PDF\_Files /Hexion/TDS/TDS%20RIMH%20137.pdf.
- Nijssen, R., G. de Winkel, J. Peeringa, and R. Date. 2007. "WMC5MW laminate lay-out of reference blade for WP 3." *Upwind Integrated Wind Turbine Design*. Accessed January 1, 2020. https://www.yumpu.com/en/document/view/37697935/wmc5mw-laminate-lay-out-of-reference-blade-for-wp-3.
- Nijssen, R. P. L. 2006. Fatigue life prediction and strength degradation of wind turbine rotor blade composites. Rep. No. SAND2006-7810P. Albuquerque, NM: Sandia National Laboratories.
- Oden, J. T., and E. A. Ripperger. 1981. Mechanics of elastic structures. Washington, DC: Hemisphere Publishing.
- Post, N. L. 2005. "Modeling the residual strength distribution of structural GFRP composite materials subjected to constant and variable amplitude tension-tension fatigue loading." Master's thesis, Virginia Tech. Accessed February 24, 2021. https://vtechworks.lib.vt.edu/handle /10919/36196.
- Post, N. L., S. W. Case, and J. J. Lesko. 2008. "Modeling the variable amplitude fatigue of composite materials: A review and evaluation of the state of the art for spectrum loading." *Int. J. Fatigue* 30 (12): 2064–2086. https://doi.org/10.1016/j.ijfatigue.2008.07.002.
- Power Line Systems. 2021. "Power transmission lines framing and configurations." Accessed February 24, 2021. http://www.powline.com/files/pls\_pole/rus/RUSModels.html#StructureSchedule.
- Re-Wind Network. 2021. "The Re-Wind network, repurposing wind blades." Accessed April 15, 2021. www.re-wind.info.
- RS. 2021. "RS composite utility poles." Accessed February 24, 2021. https://www.rspoles.com/.
- Suhail, R., J.-F. Chen, T. R. Gentry, B. Tasistro-Hart, Y. Xue, and L. C. Bank. 2019. "Analysis and design of a pedestrian bridge with decommissioned FRP windblades and concrete." In *Proc., 14th Int. Sym. on Fiber-Reinforced Polymer Reinforcement of Concrete Structures*, 1–5. Belfast, UK: IIFC. Accessed April 15, 2021. www.iifc.org/wp-content/uploads/2019/09/FRPRCS14.zip.
- Task Committee on Fiber-Reinforced Polymer Products for Overhead Utility Line Structures. 2019. MOP 104-Recommended practice for fiber-reinforced polymer products for overhead utility line structures. Reston, VA: ASCE.
- Wong, C. J., and M. D. Miller, eds. 2009. MOP 74-Guidelines for electrical transmission line structural loading. Reston, VA: ASCE.